JOURNAL OF AIRCRAFT
Vol. 42, No. 2, March–April 2005

Elastic-Blade Whirl Flutter Stability Analysis of Two-Bladed Proprotor/Pylon Systems

Beerinder Singh* and Inderjit Chopra†
University of Maryland, College Park, Maryland 20742

In axial flight, rotors with three or more blades result in constant coefficient equations of motion, but the polar asymmetry of a two-bladed rotor leads to equations of motion with periodic coefficients. Although numerous studies on whirl flutter of three-bladed rotors are available in the literature, only a few of these address the issue of two-bladed rotors. The aeroelastic stability of two-bladed proprotor/pylon/wing combinations is examined using an elastic-blade analysis. Several parametric studies have been conducted by varying the natural frequencies of the system. Results of these studies have been compared with the results of a simple rigid-blade analysis developed previously. It is shown that the rigid-blade analysis captures the important interactions between the various rotor and wing modes. However, significant differences are observed in the behavior of the whirl flutter speeds, as obtained from the two analyses, when the natural frequencies of the rotor are varied. The parametric studies show that blade elasticity affects the wing chord mode damping at flight speeds close to the flutter speed, leading to differences in the critical flight speed of the wing chord mode as compared to the rigid-blade analysis. Also, the wing beam mode, which is always stable as per the rigid-blade analysis, is found to become unstable if the wing torsional stiffness is reduced from its baseline value.

Nomenclature

h	=	pylon mast height
k_β	=	kinematic pitch–flap coupling
L	=	aerodynamic force
M	=	aerodynamic moment
N_b	=	number of blades
R	=	rotor radius
$\boldsymbol{r}$	=	position vector
T	=	kinetic energy, transformation matrix
t	=	time
U	=	elastic strain energy
u	=	axial geometric displacement
$\boldsymbol{V}$	=	velocity
v	=	chordwise (lead-lag) displacement
W	=	work done
w	=	beamwise (flap) displacement
x	=	longitudinal coordinate
x_h, y_h, z_h	=	wing-tip translational degrees of freedom
$\alpha_h, \phi_h, \zeta_h$	=	wing-tip rotational degrees of freedom
α_p	=	pylon angle
β_G	=	rotating frame flapping angle
β_p	=	rotor precone
β_T	=	fixed frame teetering angle
ϵ	=	strain
ζ	=	damping
η, ζ	=	blade cross-sectional coordinates
θ	=	blade control pitch angle
λ	=	inflow ratio
λ_i	=	induced inflow
σ	=	stress
$\hat{\phi}$	=	elastic torsion
ψ	=	blade azimuth angle
Ω	=	rotor rotational speed
$'$	=	derivative with respect to longitudinal coordinate
$*$	=	derivative with respect to azimuth angle

Presented as Paper 2003-1788 at the AIAA/ASME/ASCE/AHS/ASC 44th Structures, Structural Dynamics, and Materials Conference, Norfolk, VA, 7 April 2003; received 2 June 2003; revision received 9 January 2004; accepted for publication 12 January 2004.

*Graduate Research Assistant, Department of Aerospace Engineering, Alfred Gessow Rotorcraft Center.

†Alfred Gessow Professor and Director, Department of Aerospace Engineering, Alfred Gessow Rotorcraft Center.

I. Introduction

AEROELASTIC stability of a tiltrotor aircraft in forward flight has been the subject of considerable research since the 1960s. In high-speed axial flight, tiltrotors are subject to an instability known as proprotor whirl flutter. In this flight mode, high inflow through the rotor generates large in-plane forces as the rotor shaft pitches and yaws due to the elastic motion of the wing. With increasing airspeed, the rotor forces and the pylon/wing motion interact with each other to a point where the rotor forces become destabilizing and the rotor/pylon/wing system becomes unstable.

Most of the research on proprotor whirl flutter has focused on rotors with three or more blades. Studies conducted on the XV-3 aircraft,[1–3] the first experimental tilting proprotor aircraft, highlighted several key dynamic characteristics of a proprotor operating in high inflow. Several analytical investigations of whirl flutter were conducted during the 1960s and 1970s, using rigid pylon pivot models.[4,5] Reed[6] presented a review of these early efforts and highlighted some of the key issues associated with this instability. Hall[7] developed an analytical model to investigate the influence of various parameters, such as flight speed, pylon pitch and yaw spring rate, and pitch–flap coupling, on the stability of a rotor and pylon. The results were compared with full-scale and model tests conducted on the two-bladed XV-3 tiltrotor aircraft. The negative in-plane (H-force) damping was identified as the primary reason for proprotor instability at high forward speeds. Johnson[8] developed a mathematical model for a tiltrotor, including a modal representation of the wing, in high-speed forward flight. Analytical results obtained from this analysis showed good correlation with full-scale proprotor tests, and the analysis was later extended to include elastic blades and helicopter and conversion modes of operation.[9] Kvaternik and Kohn[10] carried out an experimental parametric investigation of whirl flutter for a proprotor mounted on a rigid pylon with flexibility in pitch and yaw. Results of this study showed that proprotor whirl flutter can be predicted with linear stability analyses using two-dimensional, quasi-steady aerodynamics for the blade loading. Nixon[11,12] conducted parametric studies for aeroelastic stability of a tiltrotor in forward flight using a finite element-based comprehensive tiltrotor

aeroelastic analysis. The effects of several design parameters, such as rotor flap and lag frequencies, blade pitch–flap coupling, wing stiffness and sweep, were examined to determine their effect on aeroelastic stability in the high-speed axial flight mode. Lag frequency tuning was found to be a practical method for increasing flutter speed in axial flight, and forward sweep of the wing was found to be destabilizing.[11,12] Srinivas et al.[13] extended this analysis to include pitch–lag coupling and antisymmetric motion of the airframe.

In recent years, numerous approaches for the improvement of tiltrotor whirl flutter boundaries have been investigated. Srinivas and Chopra,[14] Popelka et al.,[15] Corso et al.,[16] and Barkai and Rand[17] investigated the use of aeroelastic tailoring of composite wing and rotor blades to enhance whirl mode stability of a tiltrotor in forward flight. Nixon et al.[18] presented a review of the experimental and analytical efforts for stability augmentation of tiltrotors through aeroelastic tailoring of the wing and rotor blades. Srinivas et al.[13] carried out studies on improving whirl mode stability of tiltrotors by using advanced geometry blades with tip sweep and tip anhedral/dihedral. Acree et al.[19] investigated the effect of chordwise positions of the rotor blade aerodynamic center and center of gravity on stability. Rearward offsets of the aerodynamic center with respect to the blade elastic axis and pitch axis were found to be beneficial for stability, with the effect being most dominant for offsets at the outboard part of the blade. Acree[20] also analyzed the effect of blade tip sweep on whirl mode stability of the V-22 tiltrotor with a tip mass extended on a boom forward of the leading edge to compensate for the aft shift of the tip center of gravity due to sweep.

Most of the above studies were carried out on three-bladed proprotors, although Johnson[8] presented some results for a two-bladed propeller as well. Unlike a rotor with three or more blades, a two-bladed rotor lacks polar symmetry, which leads to proprotor equations of motion containing periodic coefficients. Thus, the stability analysis in the case of a two-bladed rotor is more involved. In June 1998, whirl flutter was encountered during a flight test of the Pathfinder aircraft, which was fitted with several two-bladed propellers to be used on the Helios aircraft. These aircraft, built under the Environmental Research Aircraft and Sensor Technology program, have lightweight and highly flexible wing structures and soft-mounted propellers. The simplified analysis for two-bladed rotors given in Ref. 8, when applied to the Pathfinder configuration with the Helios propellers, was unable to predict the flutter encountered in 1998. Recently, the authors presented the results of several parametric studies on the whirl flutter stability of two-bladed proprotors, using a simple rigid-blade analysis.[21,22] Because data for the Pathfinder configuration are not available in the public domain, the studies were conducted on a hypothetical, two-bladed version of the XV-15 rotor. These studies highlight the special nature of two-bladed proprotors by bringing out several key differences in their aeroelastic behavior. The analytical model used in Refs. 21 and 22 relied on prior knowledge of the blade lag frequency variation with collective pitch. Also, the blades were considered to be rigid, and blade torsional motion was not considered in the analysis. In this paper, the whirl flutter stability of two-bladed tiltrotors is examined with an elastic-blade analysis, including elastic torsion.

II. Formulation

Aeroelastic formulation for a two-bladed teetering proprotor mounted on a cantilever wing is described in this paper. The rotor blade is discretized into an arbitrary number of Euler–Bernoulli type beam finite elements. Interelement compatibility relations are satisfied using nonlinear transformations, and the formulation can handle offsets of blade section center of mass, aerodynamic center, and tension center from the elastic axis. The elastic-blade tiltrotor formulation is described in detail in Refs. 11 and 23. The tiltrotor wing is also modeled using the same Euler–Bernoulli elements as the blade, but with zero rotational speed. Hamilton's principle is used to derive the blade and wing equations of motion. This formulation for a two-bladed teetering rotor has been implemented in the comprehensive aeroelastic analysis code UMARC (Refs. 11 and 23).

A. Reference Frames

Because the wing itself is flexible, a deformed-wing reference frame is required to describe the motion at the wing tip, as shown in Fig. 1. There are six degrees of freedom at the point where the rotor pylon connects to the wing tip, three associated with translations and three with rotations. These six degrees of freedom are similar to the hub degrees of freedom in a helicopter case. These are x_h (longitudinal translation, positive aft), y_h (lateral translation, positive toward right), z_h (vertical translation, positive up), α_h (pitch rotation, positive nose down), ϕ_h (roll rotation, positive in the direction of rotor rotation) and ζ_h (yaw rotation, positive yaw to the left), as shown in Fig. 1.

The hub reference frame is offset from the wing-deformed frame by the pylon height h and is oriented in the same direction as the wing-deformed frame when the pylon angle α_p is zero (Fig. 2). The pylon angle is assumed to be a large, constant input angle, and the pylon is assumed to be rigid. The hub rotating frame rotates with the blade about the hub frame as shown in Fig. 2.

Tiltrotors commonly use a gimbal for connecting the rotor to the hub. In the hub-rotating frame, the gimbal flapping β_G adds to the rotor precone β_P as shown in Fig. 3. For a three-bladed rotor, it is convenient to treat the gimbal flapping as two orthogonal rotations,

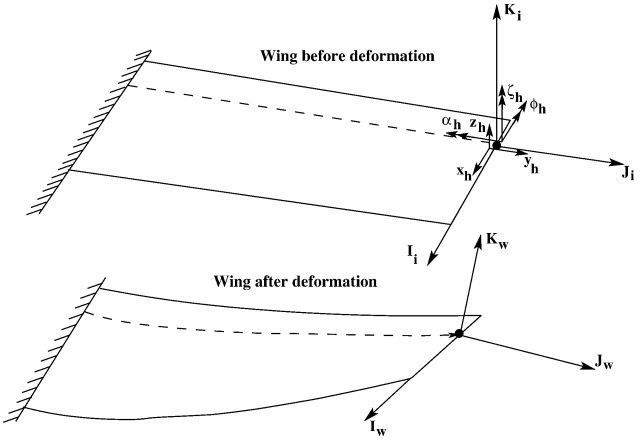

Fig. 1 Pylon reference system: pylon translations and rotations.

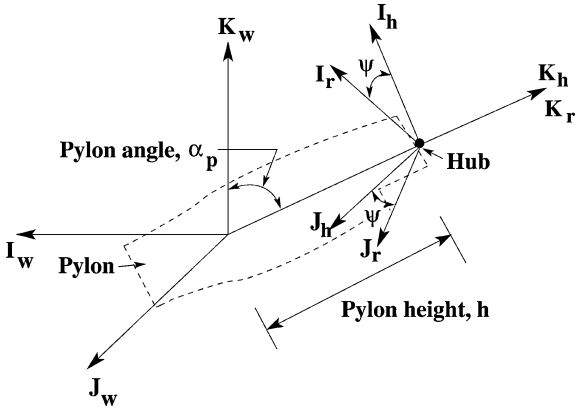

Fig. 2 Geometry of pylon and hub.

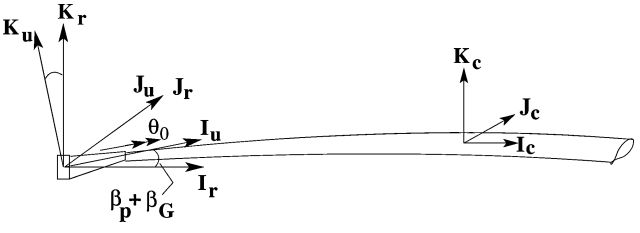

Fig. 3 Blade geometry.

β_{GC} and β_{GS}, in the fixed frame,[11,13]

$$\beta_G^{(m)} = \beta_{GC}\cos\psi_m + \beta_{GS}\sin\psi_m \tag{1}$$

where, m refers to the blade number and ψ is the azimuth.

However, for a two-bladed rotor, the preceding transformation leads to more degrees of freedom than are necessary to describe the teetering motion of the rotor. In this case,

$$\beta_G^{(m)} = \beta_T(-1)^m \tag{2}$$

where β_T is the teetering motion of the rotor. In the present analysis, the equations of motion have been derived with the rotating-frame flapping motion β_G instead of the fixed-frame flapping motions β_{GC} and β_{GS}.

The blade undeformed frame is obtained by starting from the hub rotating frame and rotating through the precone angle β_p and the flapping angle β_G as shown in Fig. 3. The blade undeformed frame is related to the blade cross-section frame through the control pitch θ_0, which includes the blade collective and cyclic pitch. The blade pitch angle is assumed to be large. Thus, there are a total of seven different coordinate systems from the inertial to the deformed system: inertial i, deformed wing w, hub fixed h, hub rotating r, undeformed blade u, blade cross section c, and deformed blade d. The transformation matrices are

$$[T_{cu}] = \begin{bmatrix} 1 & 0 & 0 \\ 0 & \cos\theta_0 & \sin\theta_0 \\ 0 & -\sin\theta_0 & \cos\theta_0 \end{bmatrix} \tag{3}$$

$$[T_{ur}] = \begin{bmatrix} \cos(\beta_p+\beta_G) & 0 & \sin(\beta_p+\beta_G) \\ 0 & 1 & 0 \\ -\sin(\beta_p+\beta_G) & 0 & \cos(\beta_p+\beta_G) \end{bmatrix} \tag{4}$$

$$[T_{rh}] = \begin{bmatrix} \cos\psi & \sin\psi & 0 \\ -\sin\psi & \cos\psi & 0 \\ 0 & 0 & 1 \end{bmatrix} \tag{5}$$

$$[T_{hw}] = \begin{bmatrix} \cos\alpha_p & 0 & \sin\alpha_p \\ 0 & 1 & 0 \\ -\sin\alpha_p & 0 & \cos\alpha_p \end{bmatrix} \tag{6}$$

$$[T_{wi}] = \begin{bmatrix} \cos\zeta_h & \sin\zeta_h & 0 \\ -\sin\zeta_h & \cos\zeta_h & 0 \\ 0 & 0 & 1 \end{bmatrix} \times \begin{bmatrix} \cos\alpha_h & 0 & \sin\alpha_h \\ 0 & 1 & 0 \\ -\sin\alpha_h & 0 & \cos\alpha_h \end{bmatrix} \times \begin{bmatrix} 1 & 0 & 0 \\ 0 & \cos\phi_h & -\sin\phi_h \\ 0 & \sin\phi_h & \cos\phi_h \end{bmatrix} \tag{7}$$

B. Deformed Blade Geometry

To derive the blade equations of motion, it is necessary to define the position vector of an arbitrary point on the deformed blade. The transformation T_{dc} defines the transformation from the blade cross-section frame to the blade deformed frame,

$$[T_{dc}] = \begin{bmatrix} 1-\dfrac{v'^2}{2}-\dfrac{w'^2}{2} & v' & w' \\ -v'C^1 & -v'w'S^1 & \left(1-\dfrac{w'^2}{2}\right)S^1 \\ -w'S^1 & +\left(1-\dfrac{v'^2}{2}\right)C^1 & \\ -w'C^1 & -v'w'C^1 & \left(1-\dfrac{w'^2}{2}\right)C^1 \\ +v'S^1 & -\left(1-\dfrac{v'^2}{2}\right)S^1 & \end{bmatrix} \tag{8}$$

where $C^1 = \cos\theta_1$ and $S^1 = \sin\theta_1$. Here v and w are the blade lag and flap deformations, respectively. Also,

$$\theta_1(s) = \theta_t(s) + \hat{\phi}(s) \tag{9}$$

where s is the local coordinate along the blade segment and θ_t is the pretwist,

C. Equations of Motion

The equations of motion are derived using Hamilton's variational principle generalized for a nonconservative system,

$$\delta\Pi = \int_{t_1}^{t_2} (\delta U - \delta T - \delta W)\,\mathrm{d}t = 0 \tag{10}$$

where δU is the variation of the elastic strain energy, δT is the variation of the kinetic energy, and δW is the work done by nonconservative forces, which are of aerodynamic origin. The variation of strain energy may be written as the sum of the variations in strain energy for the blades, hub, and wing,

$$\delta U = \left(\sum_{m=1}^{N_b} \delta U_b\right) + \delta U_h + \delta U_w \tag{11}$$

where, the subscripts b, h, and w refer to the blade, hub, and wing, respectively, and N_b is the number of blades.

1. Strain Energy

The blade strain energy formulation remains unchanged from the three-bladed case described in Refs. 11 and 13. The formulation includes nonclassical effects such as warping and transverse shear using a detailed local cross-section analysis, and the effective properties are used to characterize the global beam analysis. The variation of the elastic strain energy is given by

$$\delta U = \int_0^R \iint_A (\sigma_{xx}\delta\epsilon_{xx} + \sigma_{x\eta}\delta\epsilon_{x\eta} + \sigma_{x\zeta}\delta\epsilon_{x\zeta})\,\mathrm{d}\eta\,\mathrm{d}\zeta\,\mathrm{d}x \tag{12}$$

Strain–displacement relations are defined as

$$\epsilon_{xx} = u' + \frac{1}{2}v'^2 + \frac{1}{2}w'^2 + \frac{1}{2}(\eta^2+\zeta^2)\hat{\phi}'^2 + (\eta^2+\zeta^2)\theta_0'\hat{\phi}' - v''[\eta\cos\theta_1 - \zeta\sin\theta_1] - w''[\eta\sin\theta_1 + \zeta\cos\theta_1] + (\hat{\phi}'\lambda_T)' \tag{13}$$

$$\epsilon_{x\eta} = v_s'\cos\theta_1 + w_s'\sin\theta_1 + \left(\frac{\mathrm{d}\lambda_T}{\mathrm{d}\eta} - \zeta\right)\hat{\phi}' \tag{14}$$

$$\epsilon_{x\zeta} = w_s'\cos\theta_1 - v_s'\sin\theta_1 + \left(\frac{\mathrm{d}\lambda_T}{\mathrm{d}\zeta} + \eta\right)\hat{\phi}' \tag{15}$$

where, λ_T refers to the torsion-related out-of-plane warping terms and the subscript s refers to the shear deformation components of the lag and flap degrees of freedom.[13] Stress–strain relations are substituted into the strain energy variation, which is then integrated over the cross section of the blade to obtain the strain energy variation in terms of the blade displacements.

2. Kinetic Energy

The velocity at a point on the blade is determined by blade motion and hub motion, with the hub motion being a result of wing motion. The total velocity at a point on the blade may be expressed as

$$\boldsymbol{V} = \boldsymbol{V}_b + \boldsymbol{V}_h \tag{16}$$

where, V_b and V_h represent the contributions of the blade and hub, respectively. These contributions are determined from the position vector of an arbitrary point on the blade. In the inertial frame, the

position vector of a point on the blade can be written as

$$\boldsymbol{r} = (\{x_h, y_h, z_h\} + \{0, 0, h\}[T_{wi}] + \{(x+u), v, w\}[T_{ci}] + \{0, \eta, \zeta\}[T_{di}]) \begin{Bmatrix} \hat{I}_i \\ \hat{J}_i \\ \hat{K}_i \end{Bmatrix} \tag{17}$$

The velocity vector is given by

$$\boldsymbol{V} = \frac{\mathrm{d}\boldsymbol{r}}{\mathrm{d}t} = V_x \hat{I}_i + V_y \hat{J}_i + V_z \hat{K}_i \tag{18}$$

From this velocity vector, the kinetic energy of an arbitrary point on the blade can be determined and then integrated over the cross section to determine the total kinetic energy.

3. Blade Discretization

A 15-degree-of-freedom finite element[23] is used to discretize the equations of motion. The nodal degrees of freedom are defined as

$$\hat{q} = [u_1 \;\; u_2 \;\; u_3 \;\; u_4 \;\; v_1 \;\; v_1' \;\; v_2 \;\; v_2' \;\; w_1 \;\; w_1' \;\; w_2 \;\; w_2' \;\; \hat{\phi}_1 \;\; \hat{\phi}_2 \;\; \hat{\phi}_3]^T \tag{19}$$

The hub degrees of freedom, which are already discrete, are given by

$$\hat{x}_h = [x_h \quad y_h \quad z_h \quad \alpha_h \quad \phi_h \quad \zeta_h \quad \beta_T]^T \tag{20}$$

The following substitution is made to replace the rotating frame flapping motion β_G by the rotor teetering motion β_T:

$$\beta_G^{(m)} = \beta_T (-1)^m \tag{21}$$

Also, the equation of motion for the teeter degree of freedom is obtained from the equilibrium of flap moment about a teeter hinge,[24]

$$M_T = \sum_{m=1}^{2} (-1)^m M_y^m \tag{22}$$

where M_y^m is the flap moment at the teeter hinge due to the mth blade.

In the total energy variation, the terms that are coefficients of the blade variational degrees of freedom $\delta\hat{q}$ constitute the blade equations, whereas the terms that are coefficients of the hub variational degrees of freedom δx_h constitute the hub equations. In matrix form, the blade equations may be written as

$$\delta U_i - \delta T_i = \delta\hat{q}^T \left([M_{bb}]\ddot{\hat{q}} + [C_{bb}]\dot{\hat{q}} + [K_{bb}]\hat{q} + [M_{bh}]\ddot{\hat{x}}_h + [C_{bh}]\dot{\hat{x}}_h + [K_{bh}]\hat{x}_h - F_b \right)_i \tag{23}$$

where i represents the element number. The hub equations can be written in a similar manner,

$$\Delta = \delta\hat{q}^T \left([M_{hb}]\ddot{\hat{q}} + [C_{hb}]\dot{\hat{q}} + [K_{hb}]\hat{q} + [M_{hh}]\ddot{\hat{x}}_h + [C_{hh}]\dot{\hat{x}}_h + [K_{hh}]\hat{x}_h - F_h \right)_i \tag{24}$$

4. Wing Matrices

The 15-degree-of-freedom finite element used to discretize the rotor blade is also used to model the wing, but with zero rotational speed and with the hub motion terms neglected. For a rigid pylon, the wing-tip degrees of freedom are related to the hub motions as

$$u = y_h \tag{25}$$

$$v = -x_h \tag{26}$$

$$v' = \zeta_h \tag{27}$$

$$w = z_h \tag{28}$$

$$w' = -\phi_h \tag{29}$$

$$\phi = -\alpha_h[-2pt] \tag{30}$$

D. Aerodynamic Model

The aeodynamic model remains the same as in Refs. 11 and 13. Quasi-steady aerodynamics is used to model the blade airloads. This assumes that the blade loads at a given spanwise location are a function of the instantaneous section angle of attack. Also, the section airfoil characteristics are based on static data. Mach number effects are included as correction factors to the incompressible section lift, drag, and moment characteristics. Stall is not modeled in the present analysis. Because the blade airloads are motion dependent, they contribute to the load vector and the system mass, stiffness, and damping matrices. Local velocities on a blade section are calculated in the deformed reference frame. This is advantageous because high inflow aerodynamics, as seen in the inertial frame, can be treated as low inflow aerodynamics in the deformed frame. Specifically, induced inflow velocity and resultant angle of attack can be assumed to be small in the deformed frame, which simplifies the expressions for blade airloads to a large extent.

1. Local Blade Velocities

The blade velocity can be written as

$$\boldsymbol{V} = \boldsymbol{V}_b + \boldsymbol{V}_h - \boldsymbol{V}_a \tag{31}$$

where $\boldsymbol{V}_b$, $\boldsymbol{V}_h$, and $\boldsymbol{V}_a$ refer to the contributions of the blade, hub, and relative wind velocities, respectively. Here $\lambda = V/\Omega R$ is defined as the advance ratio, and λ_i is the induced inflow ratio. Relative wind velocity can be written as

$$\boldsymbol{V}_a = (\{\lambda, 0, 0\} + \{0, 0, -\lambda_i\}[T_{hi}]) \begin{Bmatrix} \hat{I}_i \\ \hat{J}_i \\ \hat{K}_i \end{Bmatrix} \tag{32}$$

$$\boldsymbol{r} = (\{x_h, y_h, z_h\} + \{0, 0, h\}[T_{wi}] + \{(x+u), v, w\}[T_{ci}] + \{0, \eta_r, 0\}[T_{di}]) \begin{Bmatrix} \hat{I}_i \\ \hat{J}_i \\ \hat{K}_i \end{Bmatrix} \tag{33}$$

$$\boldsymbol{V}_b + \boldsymbol{V}_h = \frac{\mathrm{d}\boldsymbol{r}}{\mathrm{d}t} = V_{bx}\hat{I}_i + V_{by}\hat{J}_i + V_{bz}\hat{K}_i \tag{34}$$

The total nondimensional velocity in the deformed frame is,

$$\boldsymbol{V}_{def} = (\{V_{bx}, V_{by}, V_{bz}\} + \{-\lambda, 0, 0\} + \{0, 0, \lambda_i\}[T_{hi}])[T_{id}] \begin{Bmatrix} \hat{I}_d \\ \hat{J}_d \\ \hat{K}_d \end{Bmatrix} \tag{35}$$

To account for kinematic pitch–flap coupling, the following substitution is made

$$\theta_1 = \theta_1 + k_\beta \beta_G \tag{36}$$

where $k_\beta = -\tan\delta_3$.

2. Airloads

Circulatory forces are calculated in the deformed frame using quasi-steady strip theory. The airloads are then transformed from the deformed to the undeformed reference frame. Noncirculatory contributions to airloads, arising from pitching and plunging motions of the airfoil section, are also accounted for.

Work done on the tiltrotor system is a result of the aerodynamic forces from the rotor and wing. The variation of the work done on the blades by the aerodynamic forces is given by

$$\delta W_b = \int_0^R \left(L_u^A \delta u + L_v^A \delta v + L_w^A \delta w + M_{\hat{\phi}}^A \delta\hat{\phi} \right) \mathrm{d}x \tag{37}$$

where L_u^A, L_v^A, L_w^A, and $M_{\hat{\phi}}^A$ are the distributed aerodynamic forces acting in the cross-section reference frame.

Similarly, with use of the forces and moments acting on the hub, the variation of the work done on the hub is given by,

$$\delta W_h = F_{x_h}\delta x_h + F_{y_h}\delta y_h + F_{z_h}\delta z_h + M_{\alpha_h}\delta\alpha_h + M_{\phi_h}\delta\phi_h + M_{\zeta_h}\delta\zeta_h + M_{\beta_G}\delta\beta_G \quad (38)$$

III. Analysis

The analysis can be broken down into two parts: coupled-trim analysis and rotor/wing stability analysis.

A. Coupled Trim Analysis

The coupled trim analysis involves simultaneous solution of the vehicle equilibrium equations and the blade steady periodic response equations. A rigid-blade trim analysis is used to predict the initial controls for the given flight condition. Based on these initial controls, the elastic-blade response equations, along with the vehicle force and moment residual equations, are solved using a Newton approach. To save computational time, the blade response equations are reduced into normal mode form, and then a finite element in time analysis is used to determine the blade steady periodic response. Wing motion is not included in the trim analysis.

B. Stability Analysis

For stability analysis, the differential equations of motion are linearized about the trim condition. The blade, hub, and wing equations for each element are expressed in terms of mass, damping, and stiffness matrices, which are assembled using standard finite element assembly procedure to obtain the mass, damping, and stiffness matrices of the entire system. The size of the tiltrotor problem, as solved using a complete finite element method, is extremely large, thus, requiring significant computational effort. This computational effort is reduced by transforming the blade equations into modal space. For this purpose, the blade normal modes are recalculated about the mean deflected position of the blade. The rotor is assumed to be in a state of autorotation, that is, the hub degree of freedom ϕ_h is not coupled to the wing vertical bending slope w' at the wing tip. Thus, the rotor rotational speed is a free degree of freedom. Johnson[8] showed that this assumption gives conservative results for whirl flutter stability.

For a two-bladed rotor, Floquet analysis is used to solve for system stability because the equations of motion are periodic even in axial flight. To reduce computational time for Floquet analysis, the wing matrices are condensed using static condensation, with only the six degrees of freedom at the wing tip being retained for analysis. In Refs. 21 and 22, it has been shown that such a condensation of the wing degrees of freedom produces no appreciable change in the stability characteristics of the system.

IV. Baseline System

The baseline configuration used in the present study resembles the full-scale, stiff-in-plane XV-15 model tested in the NASA Ames Research Center 40 × 80 ft wind tunnel.[8] Table 1 lists the properties of this system. In the present study, a two-bladed teetering rotor is analyzed, as opposed to the three-bladed gimballed rotor in Ref. 8. The baseline system has a positive pitch–flap coupling, that is, flap-up pitch-up, with a constant δ_3 of −15 deg. The finite element at the wing tip has a higher mass and moment of inertia to model the pylon.[22] For the results presented in this study, the first five rotor modes are retained in the analysis. The first three modes are predominantly flap–lag modes, whereas the last two are predominantly torsion modes. Only the high-speed, axial flight mode is analyzed in the present study.

Figure 4 shows the frequency and damping characteristics of the baseline system obtained using the present analysis. Figure 5 shows similar plots for the rigid-blade analysis presented in Refs. 21 and 22. For convenience, the analysis of Refs. 21 and 22 will be referred to as the rigid-blade analysis, whereas the present analysis will be referred to as the elastic-blade analysis. The quantity $V/\Omega R$ is referred to as the inflow ratio because this is essentially the non-dimensional inflow through the rotor. In Figures 4 and 5, β_0, β_1, and ζ_1 refer to modes that are predominantly collective flap, differential flap, and differential lag modes, respectively, whereas b, c, and t refer to the wing beamwise bending, wing chordwise bending, and wing torsion modes, respectively.

A key difference between the rigid-blade analysis and the present analysis lies in the definition of the rotor lag mode. Because of

Table 1 Baseline tiltrotor system

Property	Value
Rotor	
Hub type	Teetering
Number of blades	2
Radius	12.5 ft
Lock number	3.83
Solidity	0.089
Pitch-flap coupling ($\tan\delta_3$)	−0.268
Precone	0 deg
Tip speed	600 ft/s
Rotational speed	48 rad/s
Wing	
Semispan	16.65 ft
Chord	5.16 ft
Pylon height	4.28 ft
Beamwise stiffness	3.13×10^7 lb · ft^2
Chordwise stiffness	8.48×10^7 lb · ft^2
Torsional stiffness	1.62×10^7 lb · ft^2

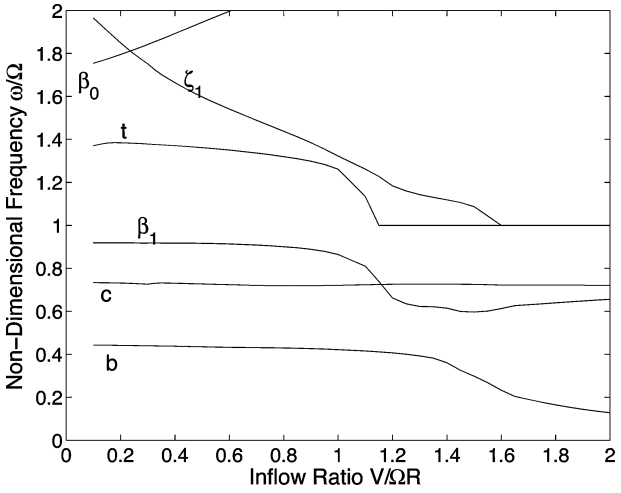

a) Frequency

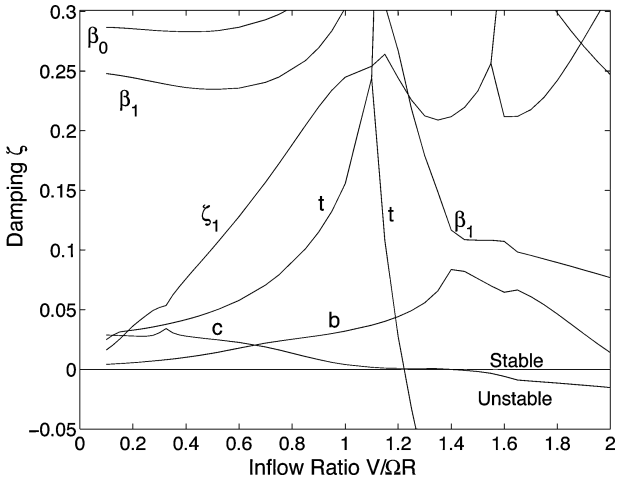

b) Damping

Fig. 4 Frequency and damping as a function of inflow ratio for baseline system (elastic-blade analysis).

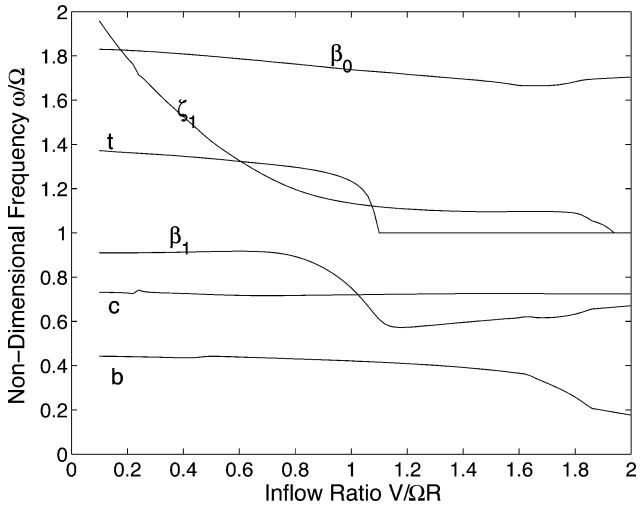

a) Frequency

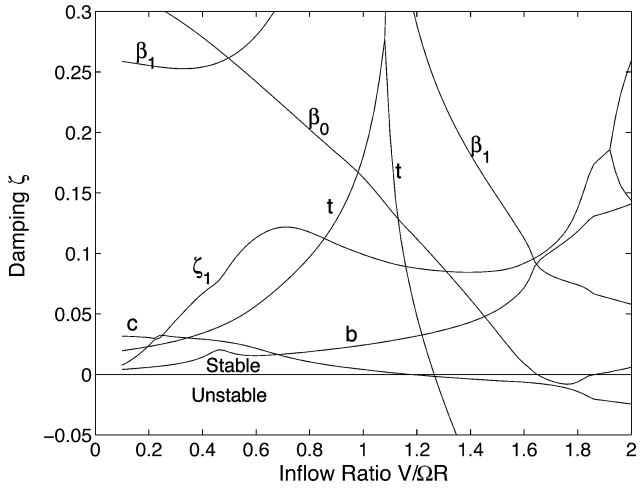

b) Damping

Fig. 5 Frequency and damping as a function of inflow ratio for baseline system (rigid-blade analysis).

the rotation of the structural principal axes, the lag frequency varies with collective pitch. In the rigid-blade analysis, this variation of the lag frequency was prescribed as an input. However, in the present analysis, the lag frequency is determined during the analysis by the variation of blade stiffness in the lag direction as the collective pitch changes. Also, in the rigid-blade analysis, the rotor lag mode was structurally uncoupled from the flap mode, but in the elastic-blade analysis the rotor lag mode is a structurally coupled lag–flap mode of the blade. However, because of its similarity with the lag mode of the rigid-blade analysis, this mode is referred to as the lag mode. Similarly, the rotor mode referred to as the β_0 mode in the elastic-blade analysis is a coupled flap–lag mode of the blade. It can be seen from Figs. 4 and 5 that the differential lag mode ζ_1 has a higher damping in the elastic-blade analysis as compared to the rigid-blade analysis, although this mode is stable in both cases.

For a two-bladed rotor, the wing torsion mode t exhibits a unique instability[21,22] in which the eigenvalue of the Floquet transition matrix corresponding to this mode becomes real, but the dominant frequency in the periodic eigenvector is 1/rev. This type of instability is referred to as a 1/rev divergence due to the similarity with constant coefficient systems, where a real positive eigenvalue implies divergence. At the point where the wing torsion mode frequency becomes 1/rev, its damping shows a split, with one part increasing and the other part decreasing. The inflow ratio at which the wing torsion mode becomes unstable is 1.22 for the elastic-blade analysis and 1.26 for the rigid-blade analysis (Figs. 4 and 5). The differential lag mode ζ_1 also shows a 1/rev divergence at high inflow ratios but remains stable in both cases.

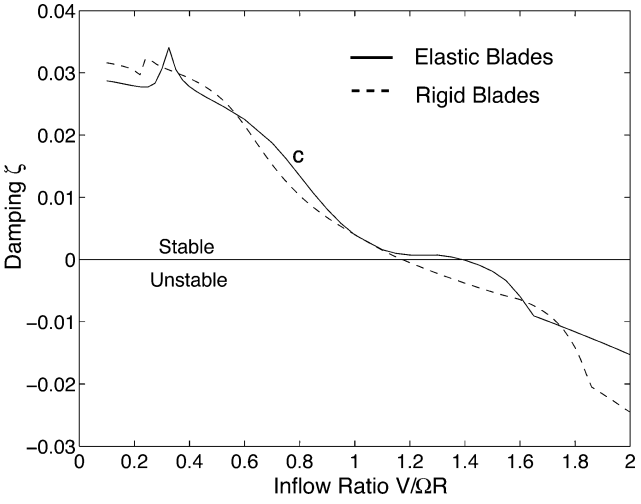

Fig. 6 Wing chord mode damping for the baseline system.

Figure 6 shows the chord mode damping obtained from the two analyses. In the rigid-blade analysis, the wing chord mode becomes unstable at an inflow ratio of 1.18, but in the elastic-blade analysis this instability occurs at an inflow ratio of 1.38.

In Refs. 21 and 22, it has been shown that the wing chord mode damping is greatly influenced by the placement of the chord mode frequency relative to the frequencies of the β_1, ζ_1, and wing torsion modes. Wing chord mode damping shows good agreement between the two analyses except at the point where the chord mode becomes unstable. The rate at which the chord mode damping reduces, just before the instability, is higher for the rigid-blade analysis leading to a lower critical inflow ratio. The peaks in wing chord mode damping (Fig. 6, $V/\Omega R \sim 0.2$) are due to its interaction with the ζ_1 mode. The elastic-blade analysis shows a larger peak in chord mode damping, indicating a greater interaction with the ζ_1 mode.

An important result of the rigid-blade analysis was that the wing beam mode remained stable for a two-bladed rotor, although this mode is critical for the stability of a three-bladed rotor.[21,22] Figure 4b shows that this remains true for the elastic-blade analysis although at high inflow ratios the wing beam mode damping obtained using the elastic blade analysis decreases. This is in contrast to the beam mode damping obtained from the rigid-blade analysis (Fig. 5b), which continues to increase, even at high inflow ratios. Thus, blade elasticity leads to a reduction in wing beam mode stability, although this mode remains the least critical mode for stability.

V. Parametric Studies

Several parametric studies have been conducted to determine the effect of key natural frequencies of the wing and rotor on the stability of the system. For comparison, the results of these studies will be shown along with the results obtained using the rigid-blade analysis.

A. Wing Frequencies

Figures 7–9 show the variation of critical inflow ratio as the wing beamwise bending EI_b, chordwise bending EI_c, and torsion GJ stiffnesses are varied independently from their baseline values. The critical inflow ratio $V_f/\Omega R$ is the inflow ratio at which the damping for a particular mode becomes zero. Although both the analyses show very similar results, there are some differences. The wing beamwise bending stiffness has a mild effect on the stability of the wing chord and torsion modes in the rigid-blade analysis (Fig. 7). However, the elastic-blade analysis shows a sudden increase in the chord mode flutter speed as EI_b factor is reduced below 1.2. This increase can be explained by looking at the variation of chord mode damping with flight speed for the baseline system, shown in Fig. 6. Between an inflow ratio of 1.1 and 1.3, the chord mode damping obtained from the elastic-blade analysis reduces by a very small

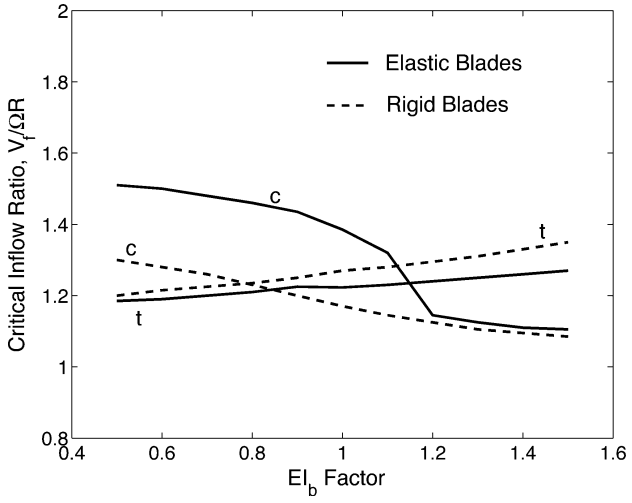

Fig. 7 Effect of wing beamwise bending stiffness on stability.

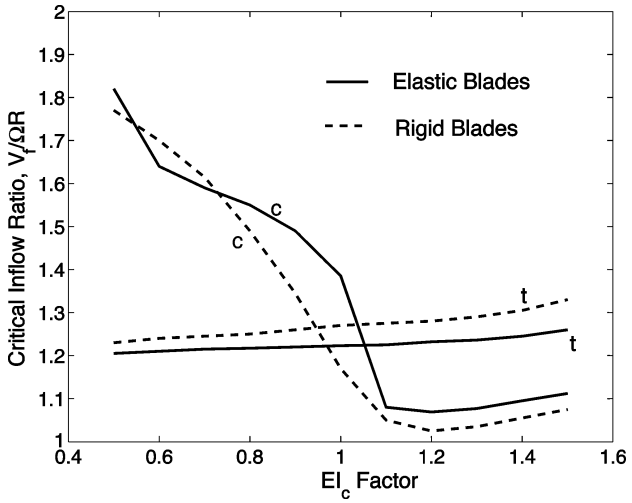

Fig. 8 Effect of wing chordwise bending stiffness on stability.

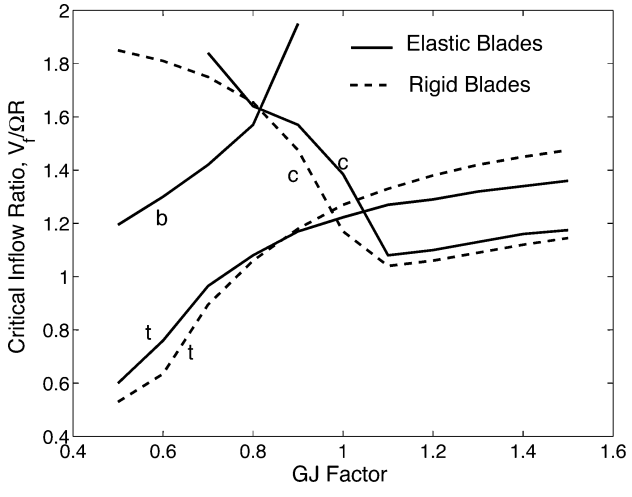

Fig. 9 Effect of wing torsional stiffness on stability.

amount, forming a plateau in the damping curve. For the baseline case, the wing chord mode becomes unstable after this plateau in its damping curve. However, as EI_b factor is increased to 1.2, the wing chord mode becomes unstable before the plateau in its damping curve, leading to a sudden reduction in the critical inflow ratio to 1.15.

In Fig. 8, the elastic-blade and rigid-blade analyses show similar trends for the critical inflow ratio as the wing chordwise bending stiffness is varied from its baseline value. The higher value of critical inflow ratio around the baseline stiffness is again due to the plateau in the chord mode damping, as discussed earlier. Wing chord mode damping is greatly influenced by the placement of the chord mode frequency relative to the frequencies of the β_1, ζ_1, and wing torsion modes.[21,22] As EI_c factor is reduced, the wing chord mode becomes more stable because its frequency moves farther away from the β_1 and ζ_1 frequencies.

Figure 9 shows that for low values of wing torsional stiffness, the wing beam mode becomes unstable in the case of the elastic-blade analysis. This difference between the elastic-blade and rigid-blade analyses is due to the behavior of beam mode damping at high advance ratios. As already discussed, the elastic-blade analysis shows a reduction in beam mode damping at high advance ratios (Fig. 4b, $V/\Omega R > 1.4$). In the rigid-blade analysis, the wing beam mode damping keeps increasing, even at high inflow ratios as shown in Fig. 5b. With a reduction in wing torsional stiffness, the wing beam mode damping starts reducing at lower inflow ratios and, thus, becomes unstable. In the rigid-blade analysis, the wing beam mode damping reduces as GJ factor is reduced, but it always remains stable.

For the elastic-blade analysis, the wing chord mode does not become unstable below a GJ factor of 0.7. This is because the wing torsion frequency exerts a stabilizing influence on the wing chord mode.[21,22] Also, as the wing torsion mode frequency reduces, the torsion mode diverges at a lower inflow ratio, leading to a significant reduction in the critical inflow ratio for the torsion mode.

B. Rotor Frequencies

The rotor frequencies, ν_β and ν_ζ, are independently varied from their baseline values by factors varying between 1.0 and 2.2. For the rigid-blade analysis of Refs. 21 and 22 the flap frequency ν_β was an input for the analysis. However, for the elastic-blade analysis, the flap frequency is determined by the spring stiffness at the teeter hinge. If there is no spring at the teeter hinge, the in vacuo flap frequency of the rotating blade is 1/rev. The relationship between the teeter spring stiffness and ν_β factor f_{ν_β} is given by

$$\omega_{\beta_0}^2 \big/ \Omega^2 = K_\beta \big/ I_\beta \Omega^2 = f_{\nu_\beta}^2 \nu_\beta^2 - 1 \tag{39}$$

where ω_{β_0} represents the flap frequency of a nonrotating blade and ν_β is the in vacuo flap frequency of the baseline rotating blade.

Figure 10 shows the effect of varying the rotor flap frequency on the critical inflow ratio. For both the rigid-blade and elastic-blade analyses, wing chord mode stability initially reduces and then increases as ν_β factor is increased from its baseline value. However, beyond a ν_β factor of 1.6, the wing chord mode flutter

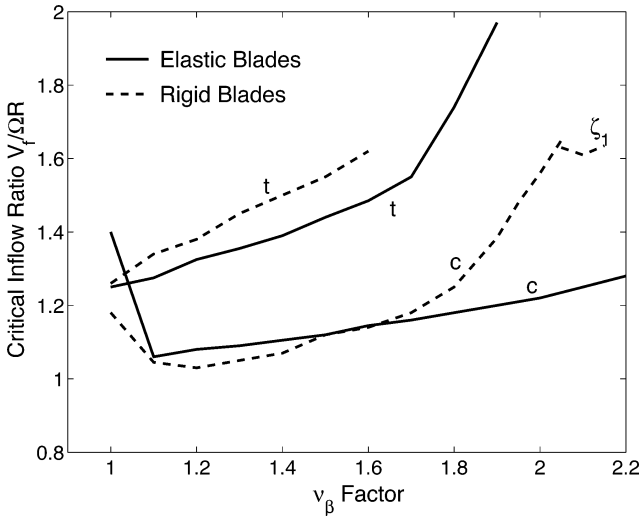

Fig. 10 Effect of flap frequency on stability.

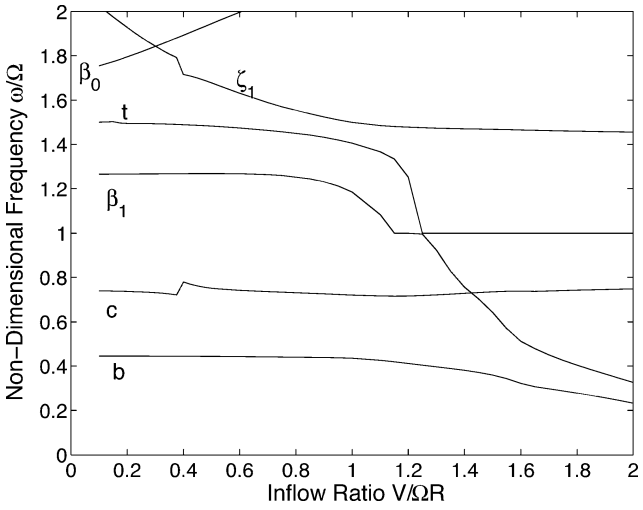

a) Frequency

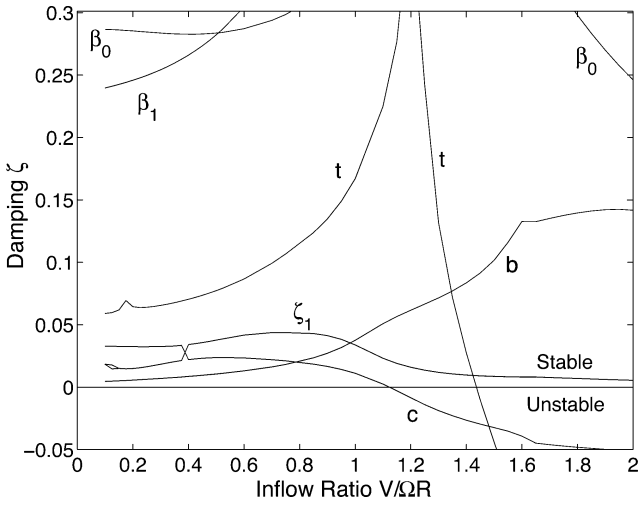

b) Damping

Fig. 11 Frequency and damping as a function of inflow ratio for ν_β factor 1.5 (elastic-blade analysis).

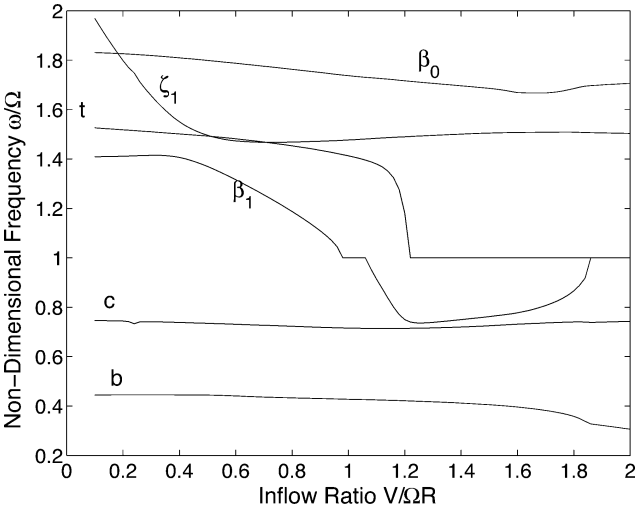

a) Frequency

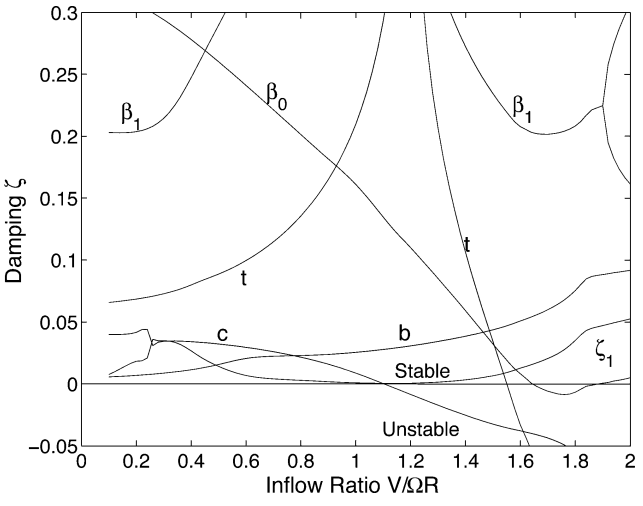

b) Damping

Fig. 12 Frequency and damping as a function of inflow ratio for ν_β factor 1.5 (rigid-blade analysis).

speed increases faster for the rigid-blade analysis. Also, the rigid-blade analysis shows an instability in the ζ_1 mode instead of the wing chord mode, beyond a ν_β factor of 2.0. The rigid-blade analysis shows a completely stable wing torsion mode beyond a ν_β factor of 1.6. However, the elastic-blade analysis shows that this mode only becomes stable for ν_β factors greater than 1.9.

The described differences can be explained by looking at the variation of the system frequencies with ν_β factor. Figures 11 and 12 show the frequency and damping characteristics of a system with ν_β factor of 1.5, obtained from the elastic-blade and rigid-blade analyses, respectively. As the spring stiffness at the teeter hinge is increased, it increases the β_1 mode frequency, which is the frequency of a coupled rotor/wing system with aerodynamics. This also causes an increase in wing torsion mode frequency at low advance ratios. However, the β_1 mode frequency obtained from the elastic-blade analysis does not increase as much as the β_1 mode frequency obtained from the rigid-blade analysis. This can be seen from the β_1 frequency at an inflow ratio of 0.1 in Figs. 11 and 12. As the β_1 mode frequency increases, it causes an increase in the torsion mode damping, which ultimately leads to the torsion mode becoming stable. Also, increasing β_1 frequency leads to a greater interaction between the β_1 and ζ_1 modes, causing a significant reduction in ζ_1 mode damping. Lesser interaction between β_1 and wing chord modes leads to an increase in the chord mode damping as well (Figs. 4, 5, 11, and 12). However, because the β_1 mode frequency of a coupled rotor/wing system with elastic blades does not increase as much as the β_1 mode frequency of a coupled system with rigid blades (Figs. 4, 5, 11, and 12), the described effects are delayed to a higher value of ν_β factor in case of the elastic-blade analysis.

Figure 13 shows the effect of varying the lag frequency by a factor varying between 1.0 and 2.2. In the rigid-blade analysis, the lag mode frequency ν_ζ, which is an input to the analysis, is multiplied by the ν_ζ factor f_{ν_ζ} for all values of the rotor collective pitch. For the elastic-blade analysis, the lag frequency increase is achieved by increasing the blade stiffnesses by a factor of $f_{\nu_\zeta}^2$. Figure 13 shows significant differences between the stability characteristics obtained using the two analyses. This is not an unexpected result because, for an elastic blade, the rotor lag mode is actually a coupled lag–flap mode of the blade, but in the rigid-blade analysis the rotor lag mode is structurally uncoupled from the flap mode.

C. Rotor Precone

Because the rigid-blade formulation does not include rotor precone, the preceding results are based on a zero precone to compare the elastic-blade and rigid-blade analyses. The full-scale XV-15 model has a precone of 2.5 deg. The elastic-blade analysis has been used to study the effect of precone on system stability. Figure 14 shows the effect of varying rotor precone angle on the critical inflow ratio. The wing torsion mode becomes unstable at slightly lower inflow ratio as the rotor precone angle is increased. Such a reduction in whirl flutter speed due to precone is also seen in three-bladed rotors.[11]

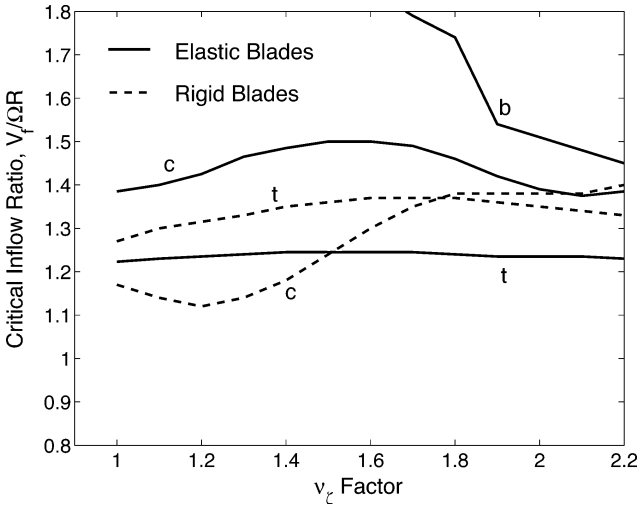

Fig. 13 Effect of rotor lag frequency on stability.

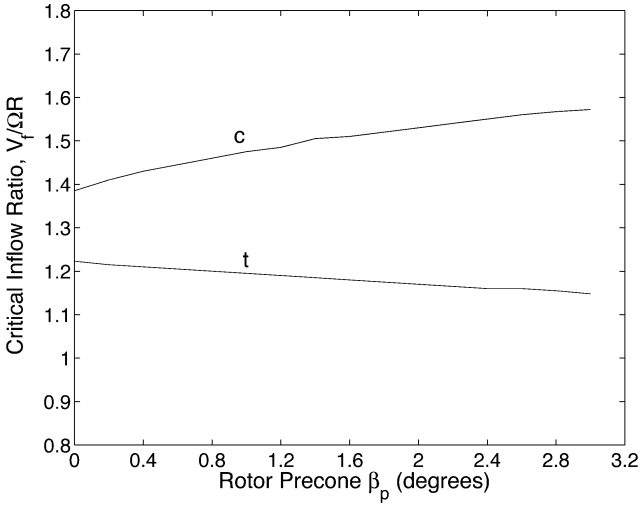

Fig. 14 Effect of rotor precone angle on stability.

VI. Summary

An elastic-blade analysis has been developed to analyze the whirl flutter stability of two-bladed proprotors. Several parametric studies have been carried out to determine the effects of various design parameters on the stability of two-bladed proprotor/pylon systems. The results have been compared to a rigid-blade analysis developed previously. Blade elasticity causes significant differences in the stability characteristics of the system when the teeter spring stiffness is increased. This is because blade elasticity limits the increase in the differential flap mode frequency as teeter spring stiffness is increased. In the elastic-blade analysis, the structurally coupled lag mode introduces significant differences in the parametric studies when the blade stiffnesses are varied. Although the two analyses show similar variations in the stability characteristics as wing stiffnesses are changed, there are some differences. Blade elasticity affects wing chord mode damping at flight speeds near the flutter speed, resulting in differences in the flutter speeds obtained from the two analyses. Although not critical for whirl flutter, the wing beam mode stability is also reduced by blade elasticity.

Acknowledgments

The authors gratefully acknowledge the support provided by the National Rotorcraft Technology Center with Dr. Yung Yu as Technical Monitor. The authors also thank Mark Nixon (U.S. Army/NASA Langley Research Center) for valuable technical discussions and Jeffrey Singleton (NASA Langley Research Center) for providing the analysis code UMARC-G.

References

[1]Koenig, D. C., Grief, R. H., and Kelly, M. W., "Full Scale Wind Tunnel Investigation of the Longitudinal Characteristics of a Tilting-Rotor Convertiplane," NASA TN D-35, 1959.

[2]Deckert, W. H., and Ferry, R. C., "Limited Flight Evaluation of the XV-3 Aircraft," U.S. Air Force Flight Test Center, Technical Rept. TR-60-4, May 1960.

[3]Quigley, H. C., and Koenig, D. C., "A Flight Study of the Dynamic Stability of a Tilting-Rotor Convertiplane," NASA TN D-778, April 1961.

[4]Reed, W. H., III, and Bland, S. R., "An Analytical Treatment of Aircraft Propeller Precession Instability," NASA TN D-659, Nov. 1961.

[5]Sewall, J. L., "An Analytical Trend Study of Propeller Whirl Instability," NASA TN D-996, 1962.

[6]Reed, W. H., III, "Propeller-Rotor Whirl Flutter: A State of the Art Review," *Journal of Sound and Vibration*, Vol. 4, No. 3, 1966, pp. 526–544.

[7]Hall, W. E., "Prop-Rotor Stability at High Advance Ratios," *Journal of the American Helicopter Society*, Vol. 11, No. 2, 1966, pp. 11–26.

[8]Johnson, W., "Dynamics of Tilting Proprotor Aircraft in Cruise Flight," NASA TN D-7677, May 1974.

[9]Johnson, W., "Analytical Model for Tilting Proprotor Aircraft Dynamics, Including Blade Torsion and Coupled Bending Modes, and Conversion Mode Operation," NASA TM X-62, Aug. 1974.

[10]Kvaternik, R. G., and Kohn, J. S., "An Experimental and Analytical Investigation of Proprotor Whirl Flutter," NASA TP-1047, 1977.

[11]Nixon, M. W., "Aeroelastic Response and Stability of Tiltrotors with Elastically Coupled Composite Rotor Blades," Ph.D. Dissertation, Dept. of Aerospace Engineering, Univ. of Maryland, College Park, MD, Sept. 1993.

[12]Nixon, M. W., "Parametric Studies for Tiltrotor Aeroelastic Stability in High Speed Flight," *Journal of the American Helicopter Society*, Vol. 38, No. 4, 1993, pp. 71–79.

[13]Srinivas, V., Chopra, I., and Nixon, M. W., "Aeroelastic Analysis of Advanced Geometry Tiltrotor Aircraft," *Journal of the American Helicopter Society*, Vol. 43, No. 3, 1998, pp. 212–221.

[14]Srinivas, V., and Chopra, I., "Validation of a Comprehensive Aeroelastic Analysis for Tiltrotor Aircraft," *Journal of the American Helicopter Society*, Vol. 43, No. 4, 1998, pp. 333–341.

[15]Popelka, D. A., Lindsay, D., Parham, T., Berry, V., and Baker, D. J., "Results of an Aeroelastic Tailoring Study for a Composite Tiltrotor Wing," *American Helicopter Society 51st Annual Forum*, May 1995.

[16]Corso, L. M., Popelka, D. A., and Nixon, M. W., "Design, Analysis and Test of a Composite Tailored Tiltrotor Wing," *American Helicopter Society 53rd Annual Forum*, April 1997.

[17]Barkai, S. M., and Rand, O., "The Influence of Composite Induced Couplings on Tiltrotor Whirl Flutter Stability," *Journal of the American Helicopter Society*, Vol. 43, No. 2, April 1998, pp. 133–145.

[18]Nixon, M. W., Piatak, D. J., Corso, L. M., and Popelka, D. A., "Aeroelastic Tailoring for Stability Augmentation and Performance Enhancements of Tiltrotor Aircraft," *Journal of the American Helicopter Society*, Vol. 45, No. 4, 2000, pp. 270–279.

[19]Acree, C. W., Peyran, R. J., and Johnson, W., "Rotor Design for Whirl Flutter: An Examination of Options for Improving Tiltrotor Aeroelastic Stability Margins," *American Helicopter Society 55th Annual Forum*, May 1999.

[20]Acree, C. W., "Effects of Rotor Design Variations on Tiltrotor Whirl-Mode Stability," *Tiltrotor/Runway Independent Aircraft Technology and Applications Specialists' Meeting of the American Helicopter Society*, March 2001.

[21]Singh, B., and Chopra, I., "Whirl Flutter Stability of Two-Bladed Proprotor/Pylon Systems in High Speed Flight," *43rd Annual SDM Conference*, April 2002.

[22]Singh, B., and Chopra, I., "Whirl Flutter Stability of Two-Bladed Proprotor/Pylon Systems in High Speed Flight," *Journal of the American Helicopter Society*, Vol. 48, No. 2, 2003, pp. 99–107.

[23]Bir, G., Chopra, I., et al., "University of Maryland Advanced Rotorcraft Code (UMARC) Theory Manual," Center for Rotorcraft Education and Research, Rept. UM-AERO 94-18, Univ. of Maryland, College Park, MD, July 1994.

[24]Yeo, H., "A Comprehensive Vibration Analysis of a Coupled Rotor/Fuselage System," Ph.D. Dissertation, Dept. of Aerospace Engineering, Univ. of Maryland, College Park, MD, 1999.